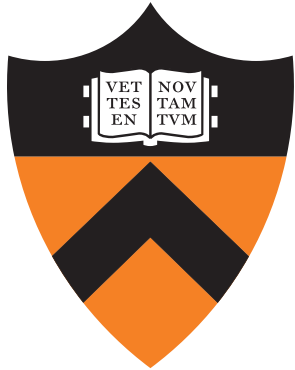


Few-Electron Quantum Dots for Electrons-on-Helium

HARSHVARDHAN KIRAN BABLA

ADVISED BY: PROF. STEPHEN A. LYON

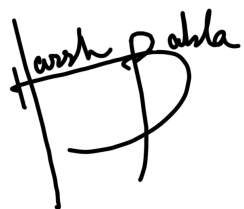


Submitted in partial fulfillment
of the requirements for the degree of
Bachelor of Science in the Engineering
Department of Electrical Engineering

PRINCETON UNIVERSITY

JANUARY 2021

I HEREBY DECLARE THAT THIS INDEPENDENT WORK REPRESENTS MY OWN
WORK IN ACCORDANCE WITH UNIVERSITY REGULATIONS.

A handwritten signature in black ink. The name "Harshvardhan" is written above "Kiran Babla". The signature is fluid and cursive, with "Harshvardhan" having a long horizontal stroke under the letters "h" and "r".

HARSHVARDHAN KIRAN BABLA

FEW-ELECTRON QUANTUM DOTS FOR ELECTRONS-ON-HELIUM

HARSHVARDHAN KIRAN BABLA

Acknowledgements

To Prof. Stephen A. Lyon, thank you for this incredible opportunity to undertake such an involved project. I truly appreciated your detailed attention and wonderful advice during our weekly meetings. Watching you generate creative ideas and quickly form intuitive explanations for complex concepts is truly inspirational. Through this past year, I've not only learned a lot about physics and engineering, but also grown my research skills and curiosity.

To Prof. Andrew A. Houck, I probably would have never found my love and passion for quantum computing if you hadn't given that wide-eyed freshman a chance to work in your lab. I very vividly remember nervously walking up to you in the E-Quad cafe, to ask you for a summer position in your lab; and you graciously invited me in, without even knowing much about me. Every conversation with you is just another an opportunity to develop a new fascination for science. Thank you for the opportunity to start research and the encouragement to pursue it into the future.

To Dr. Anthony Sigilito, thanks for your invaluable time, knowledge, of course, SnackPass coupons to Hoagie Haven. Jokes apart, I doubt that if I would've been able to make even ten percent of the progress I did, if it weren't for your guidance, support, and motivation. Your detailed knowledge from the specifics of etching all the way to electronics is incredibly impressive. I was genuinely honored to be your mentee, and am looking forward to seeing you become a great professor.

To Alex Place, your work ethic and drive for "saving lives" through quantum computing is only matched by his humility and down-to-earth nature. Thanks for teaching me most of I know about fabrication and sparking a curiosity about physics. I will miss our late night walks around campus and your endless stream of lame jokes. To Anjali Premkumar, your ability to assimilate concepts and explain them with enthusiasm is truly aspirational. I have grown so much, just learning how you break-down and understand daunting concepts. To Jeronimo Martinez, Kyle Castoria, and Sara Sussman, thanks so much for the continued motivation while working on this thesis and while applying to graduate school. To Dr. Pranav Mundada, Dr. Mattias Fitpatrick, and Dr. Christie Chiu watching your passion and fervor for research has played a huge role in shaping my scientific ambitions. Last, but certainly not least, I'd be remiss not to thank my very first research-mentor Prof. Alicia Kollar. Your talent for coming up with innovative and interesting ideas, coupled with patience while explaining complex problems has had more of an impact on my early scientific career than I can hope to express.

With gruelling classes and demanding hours of research, this may have been my toughest year at Princeton. I would never have made it through if it wasn't for the support and motivation from

my closest friends. I can not thank you enough for giving me the strength to keep going.

While I have a long ways to go, I believe Princeton has exponentially accelerated my growth as a thinker and aspiring academic. To Prof. Alejandro Rodriguez, Prof. Hansheng Diao, Prof. Hans Halvorson, Prof. Jeff Thompson, Prof. Kaushik Sengupta, Prof. Matt Weinberg, Prof. Naveen Verma, Prof. Peter Ramadge, Prof. Ravin Bhatt, Prof. Ramon van Handel, Prof. Sharad Malik, and Prof. Yuxin Chen, your classes and conversations with you have played a foundational role in broadening my horizons and teaching me how to think. I am forever grateful.

This project would not have been possible without the gracious funding from the Electrical Engineering department and the School of Engineering and Applied Sciences at Princeton. Thank you to all the faculty, administrators, and staff who organized and agreed to fund my research. To Jean Bausmith, Barbara Fruhling, and David Radcliff, thank you for making my time in the Electrical Engineering department unforgettable. To the residential staff at Forbes College, thanks for keeping me well fed and healthy through my first few years at Princeton.

Finally, to my small and happy family. Thank you for your continued support and countless sacrifices, to get me to where I am. Thank you for keeping me on my toes but also picking me up when I'm down. Dada and Maa, love you loads. Papa and Nana, this is dedicated to you :)

Contents

1	Introduction	2
2	Quantum Dots for Electrons-on-Helium	4
3	Design and Fabrication	8
3.1	Device Design	8
3.2	Fabrication Steps	10
3.3	Optimizing Fabrication Steps	15
3.3.1	Etch Tests on the Plasma-Therm APEX RIE Etcher	15
3.3.2	Dose Tests on the Heidelberg DWL 66+ Lithography System	16
4	Conclusion	20
A	Two-Dimensional Isotropic Harmonic Oscillator	21
A.1	Single-Particle Solution in Cartesian Coordinates	21
A.2	Single-Particle Solution in Polar Coordinates	23
A.3	Angular Momentum	26
A.4	Two-Particle Solution in Polar Coordinates	27
A.4.1	Decoupling the Hamiltonian	27
A.4.2	Analytical Solutions for the Internal Motion	28
A.4.3	Infinite-Field Solutions	30
A.4.4	Finite-Field Solutions	31

B Detailed Description on the Heidelberg Dose Tests	33
C Engineering and Industrial Standards	36

1

Introduction

Quantum dots are micro or nano-scale devices which serve as traps for electrons. Since quantum dots are able to confine electrons in all three spatial directions, their electronic properties show many parallels with those of atoms. As such, they're regarded as artificial atoms and their discrete energy eigenvalues are regarded as "shells". However, unlike naturally-occurring atoms the electronic potential created by quantum dots can easily be tuned by one or more voltage terminals. This allows an experimentalist to vary the number of electrons confined to a dot and conveniently scan through the periodic table. Secondly, the larger spatial dimensions of the quantum dot allow for experiments that cannot be carried out in atomic physics [1]. It is through this versatility that few-electron quantum dots prove their utility for quantum simulation.

The quantum dot's confinement potential can be approximated as a two-dimensional isotropic harmonic oscillator, with an ρ^2 cylindrical dependence [1] (where ρ is the axial distance from the center). This assumption can be verified using a finite-element package to solve the Laplace equation as will be explored in Chapter 2. A very elegant method by Schwinger shows that the radial equation of the hydrogen atom is equivalent to that of a two-dimensional harmonic oscillator [2]. Schwinger's method essentially provides a surjective homomorphism from the geometric symmetry of the hydrogen atom, $SO(3)$ to the symmetry group of the two-dimensional harmonic oscillator, $SU(2)$. The existence of this map follows from the fact that the group of unit quaternions (isomorphic to $SU(2)$) can be used to represent rotations in 3-dimensional space up to a sign [3]. This equivalence reaffirms the motivation to use quantum dots as an analog simulation for atoms.

Quantum dots are traditionally made with semiconductor heterostructures, such as InGaAs/AlGaAs [1]. These structures include a single-electron transistor (SET), which is a miniaturized resonant tunneling diode that can be driven by a small fraction of a single-electron charge [1]. These SETs allow the experimentalist to detect the electrons which tunnel out of the attached quantum dot. However, semiconductor quantum dots have a range of disadvantages. Firstly, the small effective mass in GaAs ($m^* = 0.067m_e$) results incredibly small energy values, compared to naturally occurring atomic orbitals [1]. For example ground state is 26 meV and 93 meV which are about three orders of magnitude smaller than naturally-occurring atomic orbitals [1]. Secondly, solid-state phonons notably change the spin-orbit coupling of the electrons, changing the transition energies of within the dot. Similarly, unwanted trapped charges and two-level system defects in the semiconductors change the

transition energies by warping the electrical potential around the dots. These stochastic changes in the transition energies broaden the peaks corresponding to electrons tunneling out of the dot.

On the other hand, the electrons on Helium are nearly-free. This implies that their effective mass is very close to that of a free-electron and the energy levels are a much closer match to true atomic orbitals. While “ripplons” on the liquid-Helium surface are analogous to phonons in that they physically move electrons, the much higher effective mass of the electrons on Helium implies a negligible spin-orbit coupling. Moreover, we need not worry about trapped charges on the Helium surface. As such, we expect to see much thinner peaks in current.

However, unlike semiconductor devices, it is extremely difficult to detect single electrons on Helium [4, 5]. We propose an solution to this problem by constructing large arrays (on the order of 10^6) of identical quantum dots, with the continuous metal layers and the same gate voltages. This array should allow us to perform ensemble measurements on all the dots simultaneously. Thus as we increase the voltage on the bottom metal, we expect the top-most electrons from each dot to tunnel out in unison. This would be followed by all second electrons tunneling out together, and so forth. These electrons collectively form a large current which can easily be detected. Moreover, the linewidth of the current peaks should indicate the uniformity across dots in the array. In other words, fabrication defects should widen the distribution of voltages which permit the top-most electron (and other correspondingly), hence broadening the linewidth of the transition.

This thesis is outlined as follows. Chapter 2 discusses structure and physics of the individual quantum dots. The chapter draws upon a model used by Ref. [1] to understand few-electron quantum dots within semiconductors and suggests an experiment to verify the model’s validity. Chapter 3 proposes a design for main device and a fabrication recipe to reliably and robustly construct these large arrays of identical dots. While we were able to thoroughly test these fabrication techniques, time-constraints prevented us from constructing and measuring a completed device. Finally this thesis will conclude with closing remarks and an appendix dedicated to deriving results used in Chapter 2.

2

Quantum Dots for Electrons-on-Helium

We construct our quantum dot as a two layer device separated by an insulator, as shown in Figure 2.2. A large positive voltage is applied on the bottom plate, whereas the top plate is grounded. This attracts the electrons towards the hole through which they "feel" the bottom plate's potential. The electrons can't disappear into the metal as they're confined along the z -axis by the liquid Helium surface, thus successfully trapping them within the dot.

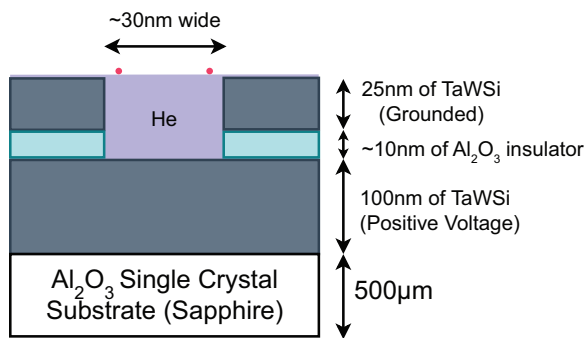


Figure 2.1: Cross-section of the proposed design of a quantum dot. A large positive voltage is applied on the bottom plate whereas the top plate is grounded. The electrons (red) are attracted towards the positive potential, but are confined to the Helium surface.

Figure 2.2 shows results from a numerical simulation of this design. We construct a device as above, and define the dielectric constants as 1.057 for Helium, 9 for Al_2O_3 , and near infinity for the conducting TaWSi. As seen in Figure 2.2(b), the potential on the liquid Helium surface is parabolic to good approximation. For low energies, the electrons experience a potential very similar to a 2D harmonic oscillator.

Much like naturally occurring atoms, the electronic structure of quantum dots is stable when its shells are completely filled. The degeneracies of orbitals within each shell along with the spin degeneracy of electrons give rise to "magic numbers" for electron occupancy, for which the systems are particularly stable. In atoms these stable structures correspond to the Noble Gasses, with electron occupancies of 2, 10, 18, 36, etc... [1].

As derived in Appendix A, the energy spectrum of the two-dimensional isotropic oscillator is given by Equation 2.1, where n quantizes the number of nodes in the wavefunction and l is the angular

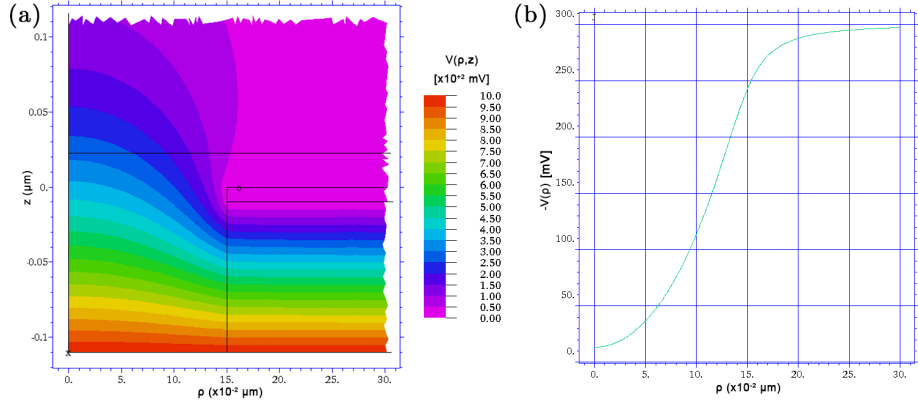


Figure 2.2: Finite-element solutions to the Laplace equation for a quantum dot under liquid Helium. Panel (a) shows the potential everywhere in space when 1V is applied on the bottom TaWSi layer and the top TaWSi layer is grounded. Panel (b) shows the potential on the surface of the Helium as a function of the axial distance, ρ . We plot the negative potential since our particle is an electron. The dip in the liquid helium surface, caused by the electron, is ignored and it is approximated as uniformly flat. These simulations were performed by Prof. Stephen Lyon.

momentum quantum number.

$$E_{n,l} = \hbar\omega(2n + |l| + 1) \quad (2.1)$$

The lowest energy state $(n, l) = (0, 0)$ can hold up to two electrons (including the spin degeneracy). The next shell has a double orbital degeneracy formed by $(0, \pm 1)$, and can contain up to 4 electrons. The third shell has a triple orbital degeneracy with $(0, \pm 2), (1, 0)$ so that it can hold up to six electrons. The lower degree of symmetry within quantum dots give rise to a lower sequence of magic numbers: $\{2, 6, 12, 20, \dots\}$.

The corresponding wavefunctions (cylindrical harmonics) are given by Equation 2.2, where $L_n^{(l)}$ are the generalized Laguerre polynomials.

$$\psi_{n,l}(\rho, \phi) = \frac{e^{il\phi}}{\rho_0} \sqrt{\frac{n!}{2\pi(n+|l|)!}} \left(\frac{\rho}{\rho_0\sqrt{2}}\right)^{|l|} e^{-\rho^2/4\rho_0^2} L_n^{(|l|)}\left(\frac{\rho^2}{2\rho_0^2}\right) \quad (2.2)$$

$$\rho_0 = \sqrt{\hbar/m\omega} \quad n \in \{0, 1, 2, \dots\} \quad l \in \{0, \pm 1, \pm 2, \dots\}$$

The relatively deep well, as seen in Figure 2.2(b), separate the dot from its surroundings, such that only highly excited electrons can thermalize out of the dot. As such, the number of electrons, N within the dot is a well defined integer. Due to this threshold, current can only flow when N electrons in the dot have sufficient energy to occupy the $N+1$ lowest possible energy states. In other words, current flows only when the top-most electron has an energy above the dot's Fermi energy, ϵ_F . As we increase the voltage of the bottom-most metal plate, the ladder of energy eigenvalues is

shifted up. We observe a sharp peak in current whenever the current top-most electron crosses the Fermi energy. This series of sharp peaks in the measured current with respect to an increase in gate voltage is seen in Figure 2.3.

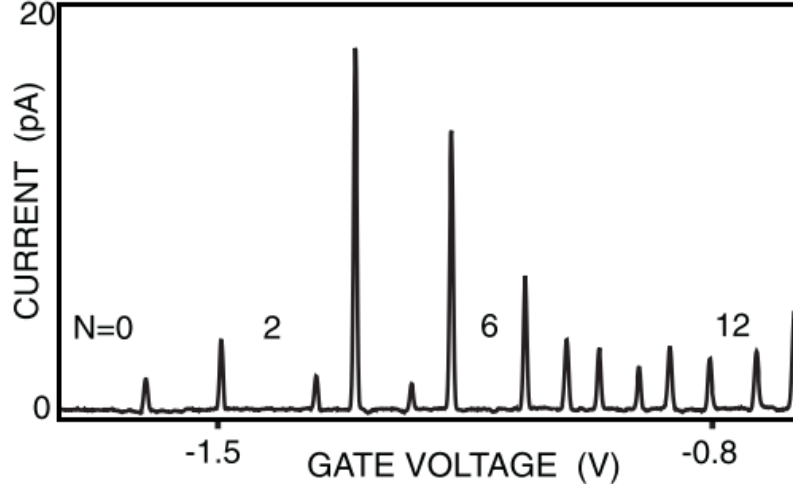


Figure 2.3: Current flowing through a two-dimensional circular quantum dot on varying the gate voltage. The first peak marks the voltage where the first electron enters the dot, and the number of electrons, N , increases by one at each subsequent peak. The distance between adjacent peaks corresponds to the addition energies. Adapted from [1].

The peaks in Figure 2.3 correspond to the transition from N to $N + 1$ electrons confined within the dot. As such, the flat portions between peaks refer to a fixed N . The distance between consecutive peaks is proportional to the addition energy E_{add} , which is the energy required to add the $(N + 1)^{th}$ electron into the dot [1]. The constant-interaction model crudely assumes that the Coulomb repulsion between electrons is independent of N . Under this assumption, the Coulomb interactions are represented as the charging energy, e^2/C , of a single electron on a capacitor, C . As such, the addition energy is given by $E_{add} = e^2/C + \Delta E$, where ΔE is the energy difference between consecutive states [1].

Let's briefly pause to motivate the CI model and justify it's validity. In Appendix A, we include the Coulomb interaction term and diagonalize the Hamiltonian for two electrons in a harmonic oscillator. However, the derivation results in the grim fact that exact solutions to this problem are only available for particular countable infinite set of oscillator frequencies. A perturbation theory approach is able to approximate the eigenenergies to good approximation [6]. Ref. [7] is able to approximately solve the three-electron problem with perturbation theory, however we were unable to find a reference which attempts to solving the many-electron problem for $N = 3$. Therefore, an scalable approximate model is absolutely neccessary. The CI model follows the atomic model for shell filling in assuming that the Coulomb repulsion between electrons is small compared to the harmonic

well. Appendix A shows that in this regime, the energy values of the two-electron system are very close to those of the single-electron problem. In our case, it is valid to assume that the electrons are far apart, as the size of the dot much larger than the spread of the electron's wavefunctions.

Ref. [1] claims that despite it's simplicity, the CI model is remarkably successful in explaining the experimental data to first order. From 2.3, observe that significantly more energy is required to add an electron to a dot with 2, 6, and 12 electrons, which correspond to the first few magic numbers for an two-dimensional isotropic harmonic oscillator. This is because the extra ΔE is only charged when an electron is added to a new shell. The first shell, $(n, l) = (0, 0)$ is doubly spin-degenerate. Therefore, adding the first electron costs $e^2/C + \Delta E$ but adding the second electron only costs e^2/C . The second shell is has double orbital and spin degeneracies and can hold up to four electrons. Hence, the only adding the third and seventh electrons costs the extra energy ΔE . This explains why the longest gaps between peaks correspond to fully filled electronic shells.

Hund's rule states that atomic shells are first filled with electrons of parallel spins until the shell is half full; then it is filled with anti-parallel spins. As such, adding an electron to a half-filled shell requires some small excess of energy. For quantum dots, the half-filling of shells happens at $N = 2, 4, 9$, and 16 . These maximally filled spin states are represented by a relatively higher peak or addition energy [1].

3

Design and Fabrication

3.1 Device Design

Unlike semiconductor devices, it is extremely difficult to detect single electrons on Helium [4, 5]. To tackle this issue we construct an array of 5.5×10^6 identical quantum dots on a centimeter-squared chip. If we perform ensemble measurements on all these dots simultaneously, we should expect to measure classical currents as the electrons would leave all of the dots simultaneously. If the dots in the array are not completely identical, which is likely to arise from fabrication defects, the linewidths of these current peaks may widen.

We measure these dots through channels connected to a very high voltage. As mentioned earlier, we remove electrons from the dots by making the bottom metal layer more negative. This pushes raises the floor of the potential, allowing the most energetic electrons to thermalize out of the dot. As we do this, we must simultaneously switch on the high positive voltage on the measurement channels, such that the electrons are pulled towards these channels. In order to minimize distorting the potential within the quantum dots, we leave $4\mu\text{m}$ of space between the dots and channels.

To ensure that all dots are collected reliably by the measurement channels, we design the device such that the channels are interspersed with the blocks of dots. Particularly, each block is an array of ten dots across and 2500 dots down. We run a measurement channel between every pair of consecutive blocks. Figure 3.1 shows a unit cell with two channels running around a single block of dots. This unit cell is tiled 220 times across the length of the chip, to form a large array of 2200×2500 dots, in total.

As elaborated in Section , it is vital that during lithography, the start and end of each stripe-width falls away from any dots. With the current design and a 20nm stripe-width, it is possible to write four unit cells before the stripe-width intersects with a block of dots. As such, we design a CAD file with only four unit cells. Then, if we tile this set-of-four within the Heidelberg's software, the tool resets the starting position of each stripe, circumventing this issue.

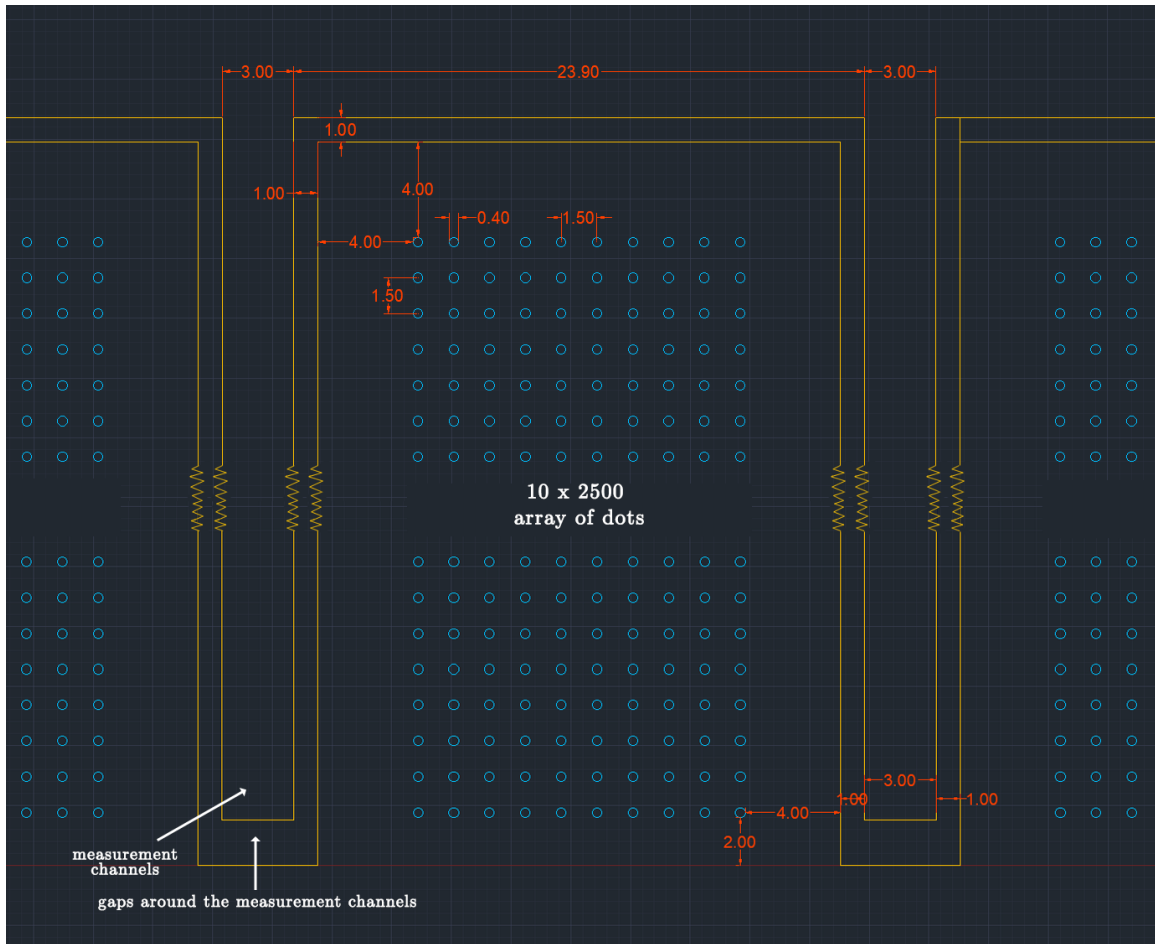
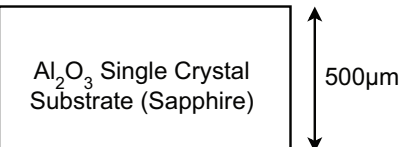
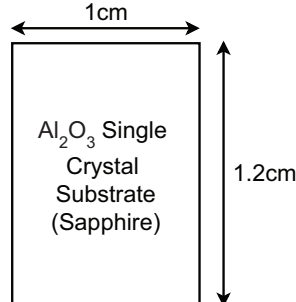
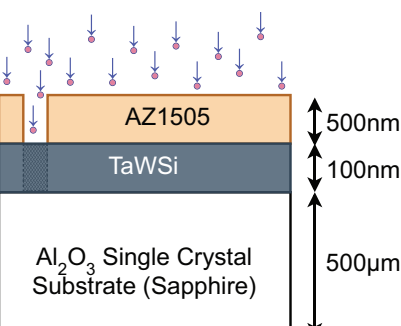
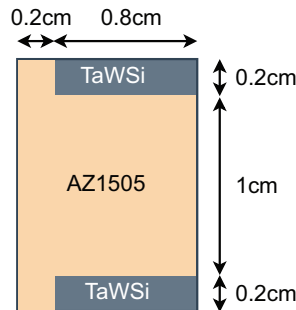


Figure 3.1: Design for the design made in AutoCAD. The boxes in yellow define the gaps around the measurement channels. The blue circles are the dots. The arrays are divided up into unit cells of 10×2500 dots, such that they can be interspersed with measurement channels. Since each unit cell is 250 times taller than it is wide, the center portion of the design has been truncated, as shown by the zig-zag lines. All measurements are in μm .

3.2 Fabrication Steps

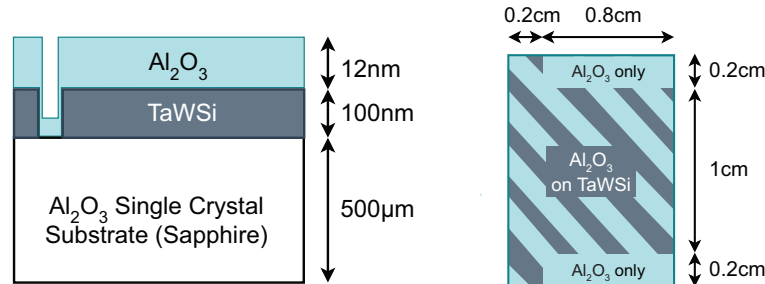
Table 3.1 explains the recipe to define bond-pads around the device. These bond-pads should allow us apply voltages to each layer individually. It is easiest to fabricate several such chips simultaneously on a large sapphire wafer. This is not only the fastest way to make several samples, but also ensures consistency across several chips. After these chips are diced, we follow Table 3.2 to define the actual device (i.e. the array of dots and streets).

Table 3.1: Fabrication Steps to Define the Bond-Pads and Dice the Devices

Steps	Cross-sectional View	Top View
1. Prepare Wafer <ul style="list-style-type: none"> (a) Starting Wafer: Al_2O_3 single crystal (sapphire) substrate. C-axis [0001]. One side CMP polished. (b) Solvent Clean: Sonicate in acetone and then in isopropanol (IPA) for 1 minutes each. Thoroughly dry off the sample. (c) Acid Clean: Soak in 3 H_2SO_4:1 H_2O_2 solution (Piranha solution) for 10 minutes. Wash thoroughly with water and then dry off the sample. 		
2. Define the Bond-Pads for the Bottom Layer of TaWSi <ul style="list-style-type: none"> (a) Deposit TaWSi using the AJA Sputterer. (1500s, 125W DC plasma, 3mTorr) (b) Define the bondpads with photolithography. (AZ1505 photoresist; 10mm writehead.) (c) Develop: Swirl in AZ300MIF developer for 1 minute. (d) Reactive-Ion Etching (RIE) to etch around the bondpads. ($\text{SF}_6 + \text{O}_2$ recipe for 1 minute) 		

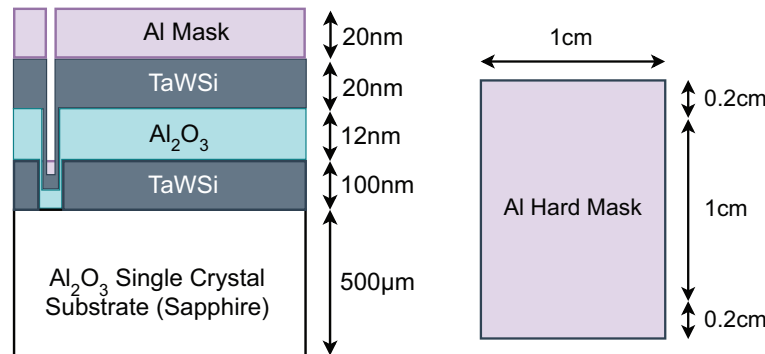
3. Grow the Insulating Layer

- (a) Strip Resist: Sonicate in PRS1000, acetone and then in IPA for 1 minute each. Thoroughly dry off the sample.
- (b) Atomic-Layer Deposition (ALD) of Al_2O_3 (100 cycles at a rate of $1.2 \text{ \AA per cycle}$).



4. Deposit Top Layer of TaWSi and Aluminum Hard Mask

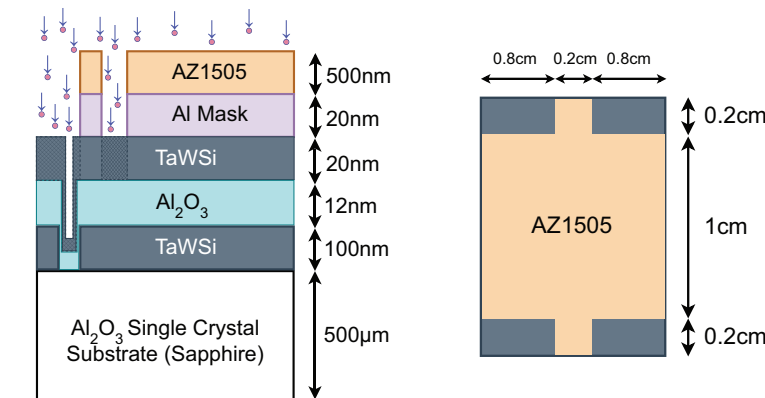
- (a) Deposit TaWSi using the AJA Sputterer. (300s, 125W DC plasma, 3mTorr)
- (b) Evaporate Aluminum using the Angstrom Nexdep. (40s at a rate of 5\AA/s . 5E-6 mTorr)



5. Define the Bond-Pads for the Top Layer

- (a) Define the bondpads with photolithography. (AZ1505 photoresist; 10mm writehead, 25% filter, 5% focus-offset, 35% intensity)
- (b) Develop: Swirl in AZ300MIF developer for 3 minutes.
Note: We develop for longer such that the developer etches through the aluminum.
- (c) RIE around the bondpads. ($\text{SF}_6 + \text{O}_2$ recipe for 30s.)

Note: A 30s etch may be longer than necessary, but we need not worry about over-etching as the Al_2O_3 acts as an etch-stop.



6. Clean Up the Wafer and Dice the Chips

- Dip in 10:1 diluted Buffered Oxide Etch (BOE) for a minute to etch any exposed oxide. Wash thoroughly with water and then dry off the sample. **Note: BOE rapidly etches through the aluminum, so it is vital to keep the protective photoresist layer during the dip.**
- Strip Resist: Sonicate in PRS1000, acetone and then in IPA for 1 minute each. Thoroughly dry off the sample.
- (Optional) Dice the rectangular ($1\text{cm} \times 1.4\text{cm}$) chips from the larger sapphire wafer.

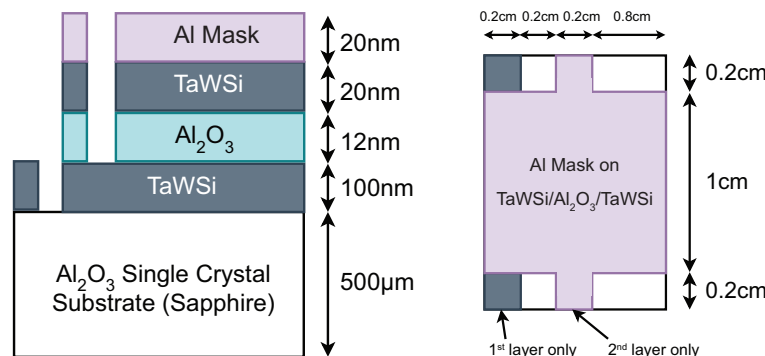
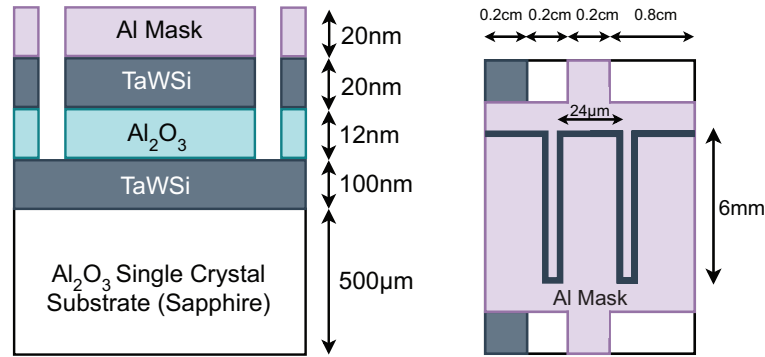


Table 3.2: Fabrication Steps for the Large Quantum-Dot Array and Measurement Channels

Steps	Cross-sectional View	Top View
1. Define the Channels into the Top TaWSi layer <ol style="list-style-type: none"> Starting Chip: Al Mask (20nm) + TaWSi layer (20nm) + Al_2O_3 insulation (12nm) + TaWSi layer (100nm), all on a sapphire substrate. As shown by Step 6 in Table 3.1. Define the channels with photolithography. (AZ1505 photoresist; 2mm writehead, 1% filter, 10% focus-offset, 35% intensity.) Develop: Swirl in AZ300MIF developer for 3 minutes. Inspect under an optical microscope. RIE through the top layer of TaWSi ($\text{SF}_6 + \text{O}_2$ recipe for 30s) <p>Note: We etch around, <u>not through</u>, the measurement channels to disconnect them from the dots.</p>		

2. Define the Channels into the Al_2O_3 Layer

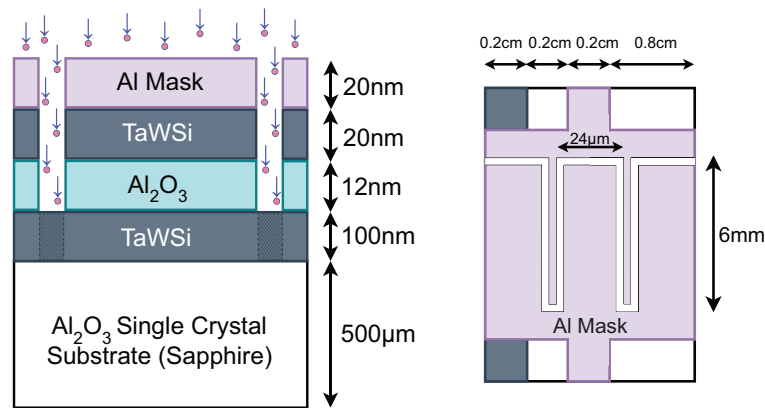
- (a) Dip in 10:1 diluted BOE for a minute to etch through the oxide layer. Wash thoroughly with water and then dry off the sample. **Note:** The HF delaminates the photoresist, so it must be removed right after.
- (b) Strip Resist: Sonicate in PRS1000, acetone and then in IPA for 1 minute each. Thoroughly dry off the sample.



3. Etch the Channels into the Bottom TaWSi Layer

- (a) For good measure, perform an oxygen descum in the APEX Metal Etcher to remove any residual oxide.
- (b) RIE through the bottom layer of TaWSi . ($\text{SF}_6 + \text{O}_2$ recipe for 1 minute).

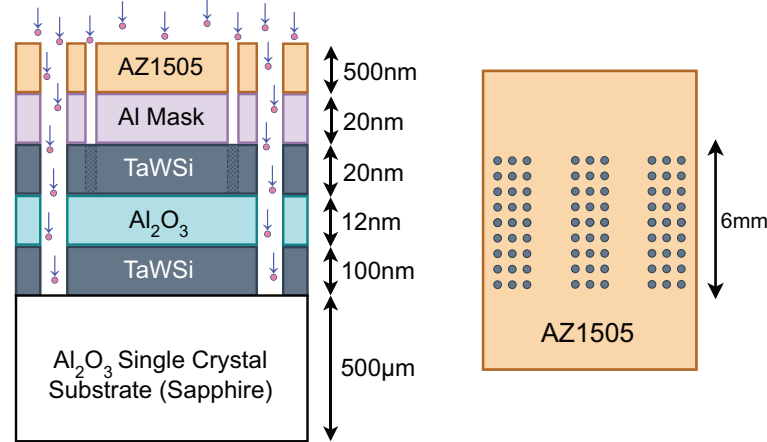
Note: The aluminum layer is used as a hard-mask (in place of the photoresist) as it is an etch-stop for the SF_6 ions.



4. Define the Array of Dots into the Top TaWSi layer

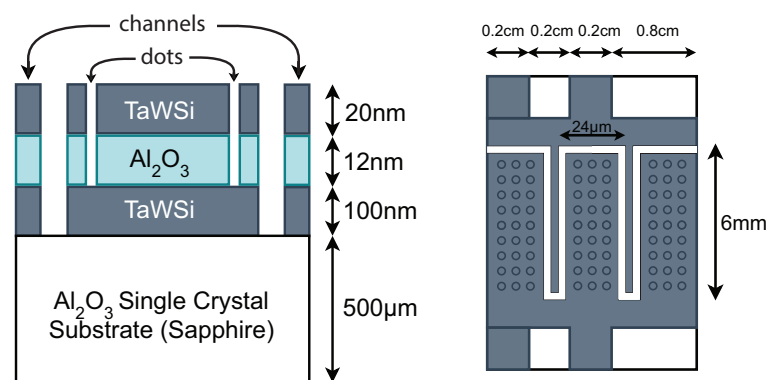
- Define the dots with photolithography. (AZ1505 photoresist; 2mm writehead, 1% + 50% filters, 7.5% focus-offset, and 20% intensity.)
- Develop: Swirl in AZ300MIF developer for 3 minutes.
- Inspect under optical microscope. Note: The dots are too small to discern optically. At best, one may be able to verify that the dot's aren't noticeably wider than expected. It may help to look through the dark-field (or ring) lighting.
- RIE through the top layer of TaWSi (SF_6+O_2 recipe for 30s)

Tip: I would recommend making two identical devices in parallel. One of which is reserved for measurement, while the other can be inspected under a Scanning Electron Microscope (SEM).



5. Clean Up the Device

- Strip Resist: Sonicate in PRS1000, acetone and then in IPA for 1 minute each. Thoroughly dry off the sample.
- Strip the Aluminum Hard Mask: Soak in AZ300MIF developer for 3 minutes. Wash thoroughly with water and then dry off the sample.
- Dip in 10:1 diluted BOE for a minute to etch any exposed oxide. Wash thoroughly with water and then dry off the sample.



3.3 Optimizing Fabrication Steps

3.3.1 Etch Tests on the Plasma-Therm APEX RIE Etcher

Etching the larger measurement channels is a reliable way to verify and improve upon our etch recipe. We came across three issues while optimizing the etch recipe:

Reaction of Chlorine with Photoresist: Initially, we thought to etch the aluminum hard mask with a BCl_3/Cl_2 chemistry RIE. While the streets were sharply defined, an unwanted debris had deposited around the streets. As seen in Figure 3.2, the debris remained in place after a solvent clean (to strip-off the photoresist), a dip in AZ300MIF developer (to strip-off the aluminum mask), and an oxygen descum. Since there wasn't any debris after developing, we knew that it's source had to be the chlorine etch. Since chlorine-based plasma are frequently used in silicon microfabrication, we suspect that the APEX's chamber may be contaminated.

In any case, we replaced this etch step with a longer developing step in AZ300MIF. 3 minutes should be sufficient to develop the resist, as well as etch through the aluminum. The sample must be stirred well while in the developer to ensure that smaller features are cleared through thoroughly.

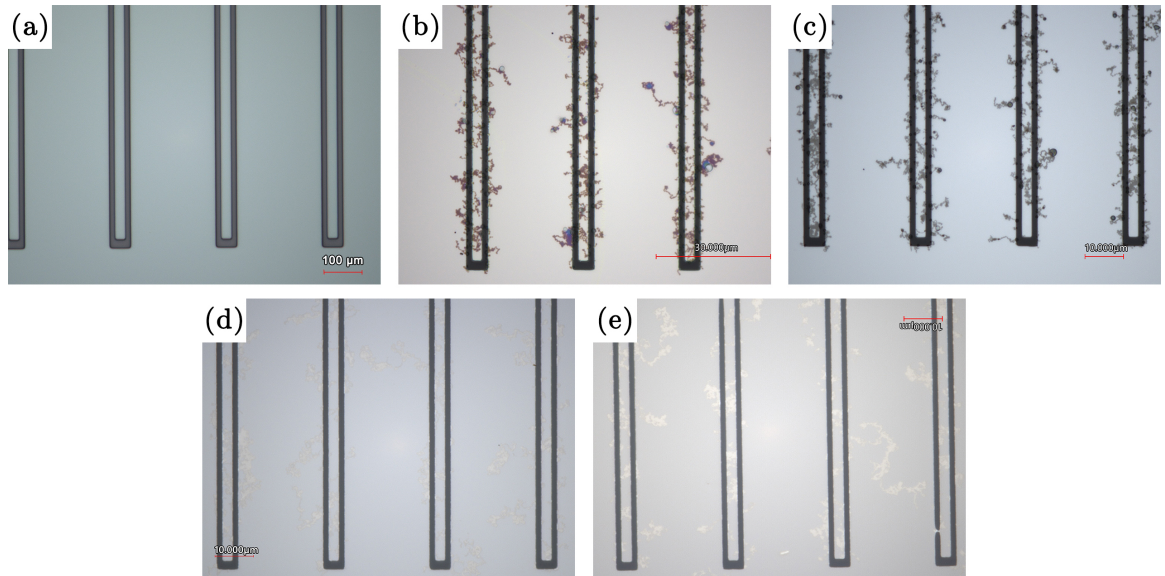


Figure 3.2: Optical microscope images of debris accruing on the sample surface as a result of the chlorine-based RIE. The panels show the sample after it has been (a) developed, (b) etched under the chlorine-based RIE, (c) solvent cleaned to remove the photoresist, (d) dipped in AZ300MIF developer for 3 minutes to remove the aluminum mask (e) exposed to an oxygen plasma to remove any residual oxide. The debris is faint in panels (d) and (e), but it hasn't completely dissapeared.

Unsuccessful Attempt at an Aggressive Etch: Al_2O_3 is known to be an etch-stop for the SF_6/O_2 etch we are using for the TaWSi. Hoping to etch through the Al_2O_3 during the same

process, we pumped Ar into the chamber along with SF₆ and O₂. We expected the argon to abrasively sputter through the oxide. However, after running the etch for varied lengths of time, we did not see an increase in the step-height of our features. This recipe needs to be studied further.

Note: The step heights were consistent across measurements on the Profilometer and the Confocal Microscope. To ensure consistency across samples, the photoresist was removed before measuring the features' profile.

After a lack of success with the aggressive etch recipe, we resorted to etching the Al₂O₃ with a dip in 10:1 diluted Buffered Oxide Etchant (BOE) for 1 minute. Since BOE etches aluminum as well, we shouldn't strip-off the resist before this step. However, BOE significantly delaminates the resist, so we must follow this step with a solvent clean.

Imprints from Previous Failed Photolithography: One of our samples underwent a faulty Heidelberg write, as the tool lost its focus during the write. Nevertheless, we stripped off the photoresist and optically verified that the aluminum hard-mask hadn't been etched. After recoating the sample with photoresist, repeating the photolithography step, and etching, we noticed that some metal had been chipped off around the measurement channels. Figure 3.3 shows optical microscope images of the sample after the photoresist and aluminum hard-mask has been stripped off. A height measurement under the confocal microscope revealed that the white regions in Figure 3.3 were about 20nm. If this measurement is accurate, we expect the top layer of TaWSi to be etched through, disconnecting the measurement channels from their bondpads. Upon further inspection, we realized that the white regions had a pattern exactly resembling the first failed write. Therefore, we suggest to strip the hard-mask and recoat the sample with aluminum whenever a photolithography step fails.



Figure 3.3: Optical microscope images of the sample with metal chipped off. These were taken after the aluminum mask had been stripped off. Therefore, the white regions were likely etched through the TaWSi.

3.3.2 Dose Tests on the Heidelberg DWL 66+ Lithography System

It was clear that we were hitting the limits of photolithography by defining sub-micron dots. However, the speed and scalability of photolithography, as well as the simplicity of our features, motivated

us to optimize this process to our needs.

We fine tuned the intensity and focus-offset parameters on the Heidelberg DWL 66+ lithography system, to minimize the size of the individual dots and maximize the consistency across the array. In order to speed up this iterative optimization, we conducted our dose tests on samples where 100nm of TaWSi was deposited on a silicon wafer. These samples could be cleaved quickly and we saved valuable time by skipping most steps enumerated in Section 3.2. Moreover, these results are can identically be implemented when constructing the actual devices, as the aluminum hard-mask prevents the dots from widening when we etch deeper into our stack.

Appendix B details this optimization process and comments on each of our samples. In summary, we encountered three key issues:

Size Gradient Across Stripe Width: The 2mm writehead on the Heidelberg has a default stripe width of $60\mu\text{m}$. However, as seen in Figure 3.4, this setting causes the size of the dots to vary along a row. To fix this issue we shrink the writehead's stripe width to $20\mu\text{m}$.

Stitching Errors: In Figure 3.4, we can see a pair of columns with abnormally wide dots. These are very likely caused by an error when stitching consecutive stripes. Even though such errors are fairly uncommon, we design our final device such that the stripes have borders far away from any dots.

Over-developing: As we shrink the writehead's strip width, the laser scans over a shorter distance and over-exposes our features. Figure 3.5 shows an image of a sample where only the stripe-width has been shrunk. The significantly more intense laser causes the features to widen until they coalesce into one another. We address this issue in two ways. First, we introduce multiple filters in front of our laser to significantly reduce its intensity. Secondly, we evaporate a thin-film (20nm) of aluminum on our top-most layer of TaWSi, to act as a hard-mask during development.

After fixing these issues, we were able to safely vary the focus-offset and intensity of the laser to minimize the size of our dots. Figure 3.6 shows SEM images of the dots as we vary the laser's intensity. Thus far, we have found the intensity of 20% with additional 1% and 50% filters to be optimal. Sweeping the focus-offset does not have a visible effect on the size of the dots, so we set it to the recommended 7.5%. These settings produce dots with a 650nm diameter. We believe that with additional filters, we can make these dots even smaller.

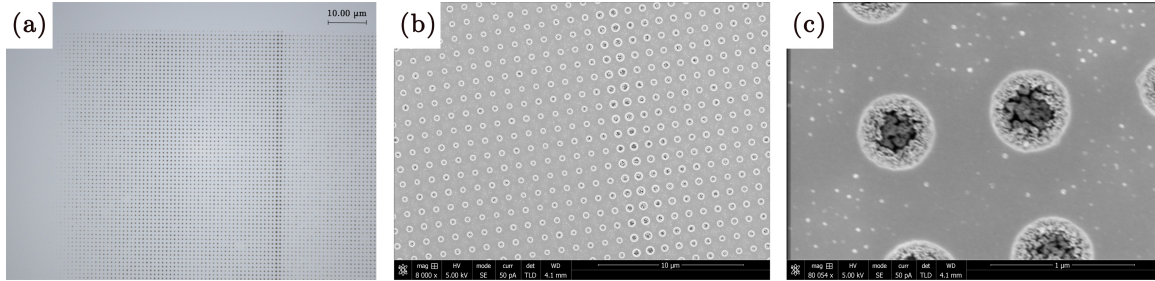


Figure 3.4: Optical (a) and SEM (b,c) images from sample HDT020. Panels (a) and (b) show a gradient in the size of the dots across a row, as well as a stitching error between consecutive stripes. Panel (c) is a magnified image of the dot. Even though the dots are of an acceptable diameter (i.e. $\approx 400\text{nm}$), the large variance in size forces us to modify the recipe. The particulates within the dot are simply a result of unintentionally etching into the silicon substrate. This issue shall not proceed when switching to sapphire substrates, as these wafers are an etch stop for the SF_6 RIE.



Figure 3.5: Optical image from sample HDT021. This sample was processed almost identically to the one shown in Figure 3.4, with mainly the stripe width changed from $60\mu\text{m}$ to $20\mu\text{m}$. We can see that the features have clearly been over-developed. The array of dots has coalesced into one large square. Upon careful inspection, a few dots are vaguely visible around the edges of the square.

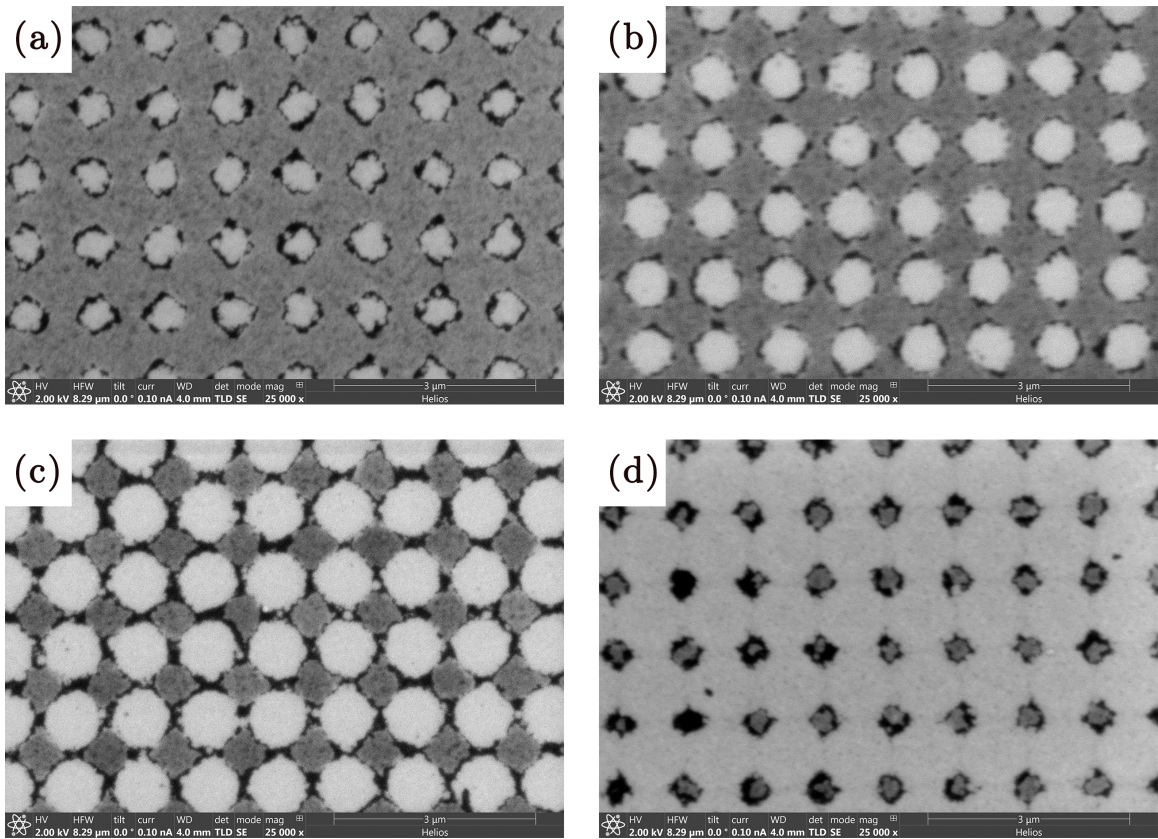


Figure 3.6: SEM images of the quantum-dot arrays from sample HDT022. The laser's intensity is swepted from (a) 20%, to (b) 30%, to (c) 45%, and to (d) 70%. Observe that increasing the intensity proportionally increases the size of these dots. The smallest dots in panel (a) are about 650nm wide, whereas in panel (d) the dots have merged to form anti-dots.

4

Conclusion

We have thus developed a recipe which to reliably and robustly fabricate large arrays of quantum dots and their corresponding measurement channels. Through rigorous iteration, we were able to push the limits of photolithography to consistently produce dots which are 500nm wide. We have also constructed a etch technique which results in sharp and well-defined features. However, time-constraints prevented us from putting these recipes together to form a completed device. Nonetheless, the path forward has already been laid out.

Even after the first set of completed devices is fabricated and measured, in many ways, the project would have only begun. Being able to construct and measure quantum wells for nearly-free electrons (i.e. electrons on liquid Helium) could open a new door into quantum computing and quantum simulation. We may be able to improve on our design by constructing a three-layer device, where electrons escape through tunneling rather than thermalization. Moreover, these devices would allow us better control to shape the dot's potential well to better approximate a harmonic oscillator. We could simulate diatomic molecules by coupling the potentials between adjacent dots. Of course, the holy grail would be to construct even narrower dots through electron-beam lithography, and hopefully trap single electrons for electron-spin-resonance measurements.

A

Two-Dimensional Isotropic Harmonic Oscillator

In general, the harmonic oscillator in two-dimensions is described by Equation A.1.

$$V(x, y) = \frac{1}{2}m\omega_1^2x_1^2 + \frac{1}{2}m\omega_2^2x_2^2 \quad (\text{A.1})$$

where the x_1 and x_2 directions align with the potential's major and minor axes. Quantum dots have rotational symmetry around the center which implies that the potential is isotropic, $\omega_1 = \omega_2$. Thus, we can rewrite the potential in terms of $\rho = \sqrt{x_1^2 + x_2^2}$.

$$V(\rho) = \frac{1}{2}m\omega^2\rho^2 \quad (\text{A.2})$$

A.1 Single-Particle Solution in Cartesian Coordinates

The Hamiltonian in Cartesian coordinates can be written as a sum of 1D harmonic oscillators, as in Equation A.3. As such, we can express it in terms of the number-operators in each direction, $\hat{a}_j^\dagger \hat{a}_j$ for $j \in \{1, 2\}$ [8].

$$H = \left[\frac{1}{2m}\hat{p}_1^2 + \frac{1}{2}m\omega^2\hat{x}_1^2 \right] + \left[\frac{1}{2m}\hat{p}_2^2 + \frac{1}{2}m\omega^2\hat{x}_2^2 \right] = \hbar\omega(\hat{a}_1^\dagger \hat{a}_1 + \hat{a}_2^\dagger \hat{a}_2 + 1) \quad (\text{A.3})$$

$$\text{where } \hat{a}_j = \sqrt{\frac{m\omega}{2\hbar}} \left(\hat{x}_j + \frac{i}{m\omega}\hat{p}_j \right) \quad ; \quad j \in \{1, 2\}$$

This implies that the Hamiltonian must be simultaneously diagonal with both number operators. This is easily realized by describing the eigenstates as a product of the 1D harmonic wavefunctions in both directions: $\psi_{n_1, n_2}(x_1, x_2) = X_{n_1}^{(1)}(x_1)X_{n_2}^{(2)}(x_2)$. These states are indexed by the eigenvalues, n_1, n_2 , of the two number operators. These quantum numbers correspond to the number of excitations (or equivalently the number of non-interacting electrons) in the x_1 and x_2 directions respectively. Recall that the 1D harmonic wavefunctions are given as in Equation A.4. The corre-

sponding eigenvalues follow from the structure of the Hamiltonian, $E_{n_1, n_2} = \hbar\omega(n_1 + n_2 + 1)$.

$$\begin{aligned} X_0^{(j)} &= \left(\frac{m\omega}{\pi\hbar}\right)^{1/4} \exp\left(-\frac{m\omega}{2\hbar}x_j^2\right) \\ X_n^{(j)} &= \frac{1}{\sqrt{n!}} \left(\hat{a}_j^\dagger\right)^n X_0^{(j)} = \frac{1}{\sqrt{2^n n!}} \left(\frac{m\omega}{\pi\hbar}\right)^{1/4} \exp\left(-\frac{m\omega}{2\hbar}x_j^2\right) H_n\left(\sqrt{\frac{m\omega}{\hbar}}x_j\right) \end{aligned} \quad (\text{A.4})$$

where $H_n(z)$ are the Hermite polynomials.

Figures A.1 and A.2 show some of the 2D wavefunctions and the energy spectrum respectively. Note that just as in the 1D harmonic oscillator, these wavefunctions are purely real. Observe that the n^{th} state has a $(n+1)$ -fold orbital degeneracy. Since each state can hold two-electrons of opposite spin, the first shell can hold up to two electrons. Similarly, the second shell can hold up to four electrons, the third shell can hold up to six electrons, and so on. These occupancies imply the magic number series: $\{2, 6, 12, 20, 30, \dots\}$ [1].

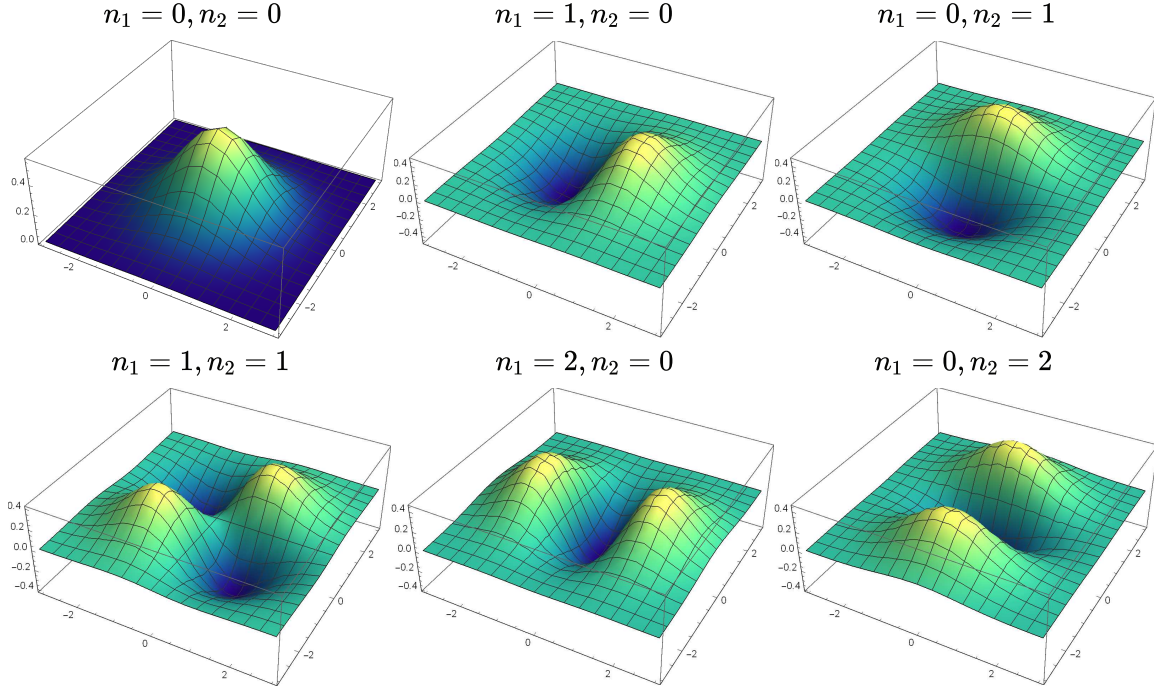


Figure A.1: Wavefunctions for the 2D isotropic harmonic oscillator solved within the Cartesian coordinates. The wavefunctions are indexed by the number eigenvalues, n_1 and n_2 , corresponding to the number of excitations in x_1 and x_2 directions respectively. Generated using Mathematica for $m = 1\text{kg}$, $\omega = 1\text{s}^{-1}$, $\hbar = 1\text{Js}$.

$\hbar\omega$	<u>(4, 0)</u>	<u>(3, 1)</u>	<u>(2, 2)</u>	<u>(1, 3)</u>	<u>(0, 4)</u>
$2\hbar\omega$		<u>(3, 0)</u>	<u>(1, 2)</u>	<u>(2, 1)</u>	<u>(0, 3)</u>
$3\hbar\omega$		<u>(2, 0)</u>	<u>(1, 1)</u>	<u>(0, 2)</u>	
$4\hbar\omega$			<u>(1, 0)</u>	<u>(0, 1)</u>	
$5\hbar\omega$				<u>(0, 0)</u>	

Figure A.2: Energy spectrum of the 2D isotropic harmonic oscillator solved within the Cartesian coordinates. The states are represented as a tuple of quantum numbers (n_1, n_2) . The spectrum is shown as a tree, where the left and right children correspond to adding an excitation in x_1 and x_2 respectively. Observe that n^{th} state is $(n + 1)$ -fold degenerate, where n is zero-indexed.

A.2 Single-Particle Solution in Polar Coordinates

Note that the 2D isotropic harmonic oscillator has rotational symmetry in both the potential and boundary condition. As seen in Equation A.2 the potential has no dependence on $\phi = \arctan(y/x)$. At first glance, it may seem surprising that the probability-density of the excited-states $\psi_{n_1, n_2}(x_1, x_2)$, described above, break this rotational symmetry.

However, recall that any linear combination of the degenerate states are also stationary states with the same energy. For example, the states $\psi_{1,0}(x_1, x_2)$ and $\psi_{0,1}(x_1, x_2)$ form the cylindrically symmetric linear combinations $\psi_{1,\pm} = \frac{1}{\sqrt{2}}(\psi_{1,0} \pm i\psi_{0,1})$. Figure A.3 illustrates the magnitude of either $\psi_{1,\pm}$. The azimuthal (ϕ) dependence only affects the phase of the wavefunction.

$$\psi_{1,\pm}(\rho, \phi) \propto (x_1 \pm ix_2)e^{-\alpha(x_1^2 + x_2^2)/2} = \rho e^{\pm i\phi} e^{-\alpha\rho/2} \quad (\text{A.5})$$

We can explicitly solve the Schrödinger equation in polar coordinates by assuming the separable

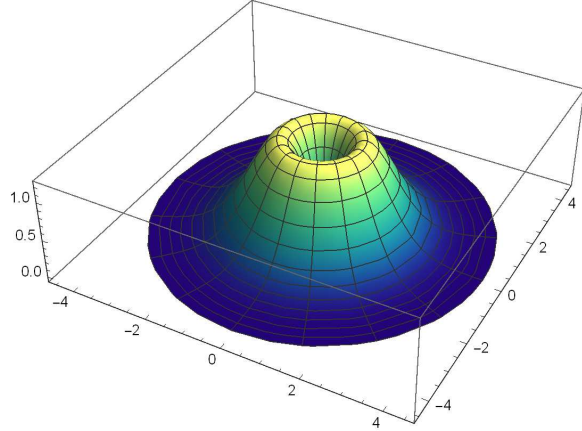


Figure A.3: The magnitude of the first excited circular harmonics, $\psi_{1,\pm} = \psi_{1,0} \pm i\psi_{0,1}$.

solution $\psi(\rho, \phi) = R(\rho)\Phi(\phi)$. The derivation is as below.

$$\begin{aligned} E\psi(\rho, \phi) &= -\frac{\hbar^2}{2m} \left[\frac{1}{\rho} \frac{\partial}{\partial \rho} \left(\rho \frac{\partial}{\partial \rho} \right) + \frac{1}{\rho^2} \frac{\partial^2}{\partial \phi^2} \right] \psi(\rho, \phi) + V(\rho)\psi(\rho, \phi) \\ 0 &= \frac{\hbar^2}{2m\rho^2} \left[\frac{\rho}{R(\rho)} \frac{d}{d\rho} \left(\rho \frac{dR}{d\rho} \right) + \frac{1}{\Phi(\phi)} \frac{d^2\Phi}{d\phi^2} \right] + [E - V(\rho)] \\ \frac{1}{\Phi(\phi)} \frac{d^2\Phi}{d\phi^2} &= \frac{\rho}{R(\rho)} \frac{d}{d\rho} \left(\rho \frac{dR}{d\rho} \right) + \frac{2m\rho^2}{\hbar^2} [E - V(\rho)] \end{aligned}$$

The left-hand side is only a function of ϕ , whereas the right-hand side is just a function of ρ . As such, we can equate each side to a constant, $-l^2$. First, let's consider the left-hand side.

$$\frac{1}{\Phi(\phi)} \frac{d^2\Phi}{d\phi^2} = -l^2 \implies \Phi_l(\phi) = e^{il\phi} \quad (\text{A.6})$$

Where the values of l appear in positive-negative pairs. The periodic boundary condition, $e^{\pm il\phi} = e^{\pm i2\pi l\phi}$ constrains l to be an integer. This solution ensures that the probability density is rotationally symmetric about the origin. Intuitively, the system can be envisioned as consisting of "quanta" with positive or negative orbital angular momentum. This is explored further in Section A.3 [8].

Next, we solve the radial equation, substituting in the harmonic potential.

$$0 = \left[\frac{d^2}{d\rho^2} + \frac{1}{\rho} \frac{d}{d\rho} - \frac{l^2}{\rho^2} \right] R(\rho) + \frac{2m}{\hbar^2} \left[E - \frac{1}{2} m\omega^2 \rho^2 \right] R(\rho) \quad (\text{A.7})$$

The solutions to this differential equation involve the generalized Laguerre polynomials, $L_n^{(l)}(z) = z^{-l}(\partial_z - 1)^n z^{n+l}/n!$ [1].

$$R(\rho) = \frac{1}{\rho_0} \sqrt{\frac{n!}{2\pi(n+|l|)!}} \left(\frac{\rho}{\rho_0 \sqrt{2}} \right)^{|l|} e^{-\rho^2/4\rho_0^2} L_n^{(l)} \left(\frac{\rho^2}{2\rho_0^2} \right) \quad (\text{A.8})$$

where $\rho_0 = \sqrt{\hbar/m\omega}$ is the characteristic length. The solutions are well-behaved for non-negative integers n :

$$n = \frac{1}{2} [|l| + 1 - \frac{E}{\hbar\omega}] \geq 0$$

In summary, the circular harmonics and the corresponding energy eigenvalues are given by Equations A.9 and A.10. The lowest energy state $(n, l) = (0, 0)$ can hold up to two electrons (including the spin degeneracy). The next shell has a double orbital degeneracy formed by $(0, \pm 1)$, and can contain up to 4 electrons. The third shell has a triple orbital degeneracy with $(0, \pm 2), (1, 0)$ so that it can hold up to six electrons. As expected, the resulting magic numbers, $\{2, 6, 12, \dots\}$ match those from

the Cartesian solution.

$$\psi_{n,l}(\rho, \phi) = \frac{e^{il\phi}}{\rho_0} \sqrt{\frac{n!}{2\pi(n+|l|)!}} \left(\frac{\rho}{\rho_0\sqrt{2}}\right)^{|l|} e^{-\rho^2/4\rho_0^2} L_n^{(|l|)}\left(\frac{\rho^2}{2\rho_0^2}\right) \quad (\text{A.9})$$

$$E_{n,l} = \hbar\omega(2n + |l| + 1) \quad (\text{A.10})$$

$$\rho_0 = \sqrt{\hbar/m\omega} \quad n \in \{0, 1, 2, \dots\} \quad l \in \{0, \pm 1, \pm 2, \dots\}$$

Figure A.4 shows some of the radial wavefunctions and their respective energies. We see that l sets the size of the dip at the origin and the radial extent of the wavefunction, whereas n represents the number of nodes in the radial direction [1].

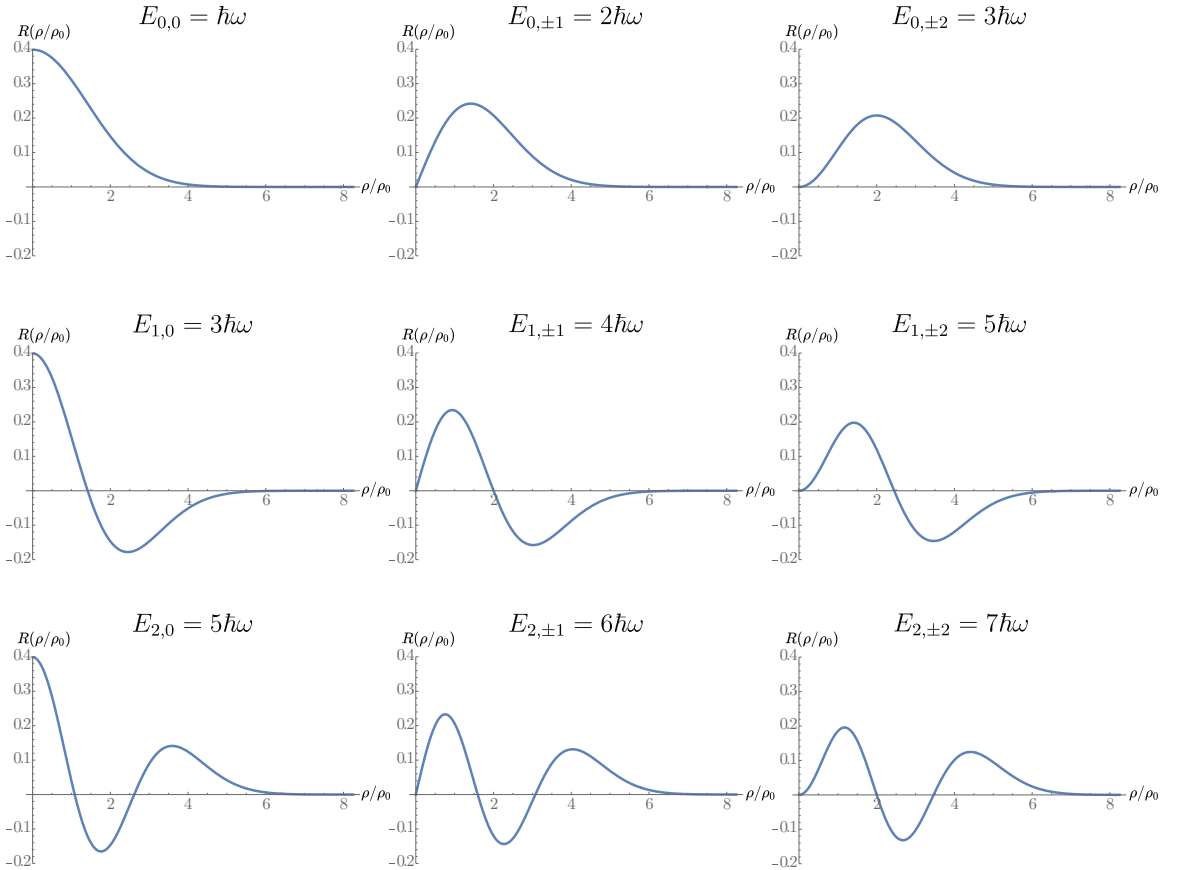


Figure A.4: The radial component for some of the wavefunctions and their corresponding energy values. The x -axis has been scaled to units of ρ_0 . The wavefunctions are indexed as (n,l) . The quantum number n increases from top to bottom, whereas l increases from left to right. Generated using Mathematica.

A.3 Angular Momentum

We briefly stated that the quantum number, l represents the number of orbital angular momentum quanta in the system. We can verify this explicitly by deriving the angular momentum operator in cylindrical coordinates for central potential, $\mathbf{r} = \rho\hat{\rho}$ [8].

$$\frac{\hat{\mathbf{L}}}{-i\hbar} = \mathbf{r} \times \nabla = \rho\hat{\rho} \times \left[\hat{\rho} \frac{\partial}{\partial\rho} + \hat{\phi} \frac{1}{\rho} \frac{\partial}{\partial\phi} + \hat{z} \frac{\partial}{\partial z} \right] = \hat{z} \frac{\partial}{\partial\phi} - \hat{\phi}\rho \frac{\partial}{\partial z} \quad (\text{A.11})$$

Since our potential is independent of z , the angular momentum operator is $\hat{L} = -i\hbar \frac{\partial}{\partial\phi}$. Equation A.12 shows that circular harmonics are in fact eigenstates of the angular momentum operator, with eigenvalues $\hbar l$.

$$\hat{L} \psi_{n,l}(\rho, \phi) = -i\hbar R_{n,l}(\rho) \frac{\partial}{\partial\phi} \Phi_l(\phi) = \hbar l \psi_{n,l}(\rho, \phi) \quad (\text{A.12})$$

Since the circular harmonics simultaneously diagonalize the Hamiltonian as well as the angular momentum, we know that the two operators commute. In other words, the angular momentum is conserved for the circular harmonics. This agrees with Noether's theorem, which states that a rotationally-symmetric Hamiltonian conserves angular momentum [9].

We can derive the same result independent of the coordinate system. Recall that the position and momentum operators can be defined in terms of the Cartesian bosonic operators [9].

$$\hat{x}_j = \sqrt{\frac{\hbar}{2m\omega}} (\hat{a}_j^\dagger + \hat{a}_j) \quad \hat{p}_j = i\sqrt{\frac{m\omega\hbar}{2}} (\hat{a}_j^\dagger - \hat{a}_j) \quad (\text{A.13})$$

where $j \in 1, 2$. This allows us to write the Hamiltonian and angular momentum operators in terms of the bosonic operators.

$$\hat{H} = \hbar\omega (\hat{a}_1^\dagger \hat{a}_1 + \hat{a}_2^\dagger \hat{a}_2 + \hat{\mathbb{I}}) \quad (\text{A.14})$$

$$\begin{aligned} \hat{L}_z &\equiv \hat{x}_1 \hat{p}_2 - \hat{x}_2 \hat{p}_1 \\ &= -\frac{1}{2}i\hbar \left[(\hat{a}_1 + \hat{a}_1^\dagger)(\hat{a}_2 - \hat{a}_2^\dagger) - (\hat{a}_2 + \hat{a}_2^\dagger)(\hat{a}_1 - \hat{a}_1^\dagger) \right] \\ &= -i\hbar (\hat{a}_1^\dagger \hat{a}_2 - \hat{a}_2^\dagger \hat{a}_1) \end{aligned} \quad (\text{A.15})$$

$$= \hbar \begin{bmatrix} \hat{a}_1^\dagger & \hat{a}_2^\dagger \end{bmatrix} \begin{bmatrix} 0 & -i \\ i & 0 \end{bmatrix} \begin{bmatrix} \hat{a}_1 \\ \hat{a}_2 \end{bmatrix} \quad (\text{A.16})$$

where we've used the commutator identities, $[\hat{a}_j, \hat{a}_k^\dagger] = \delta_{j,k}$ and $[\hat{a}_j, \hat{a}_k] = [\hat{a}_j^\dagger, \hat{a}_k^\dagger] = 0$. Diagonalizing the matrix in Equation A.16 yields a linearly transformed set of bosonic operators for the spherical

harmonics.

$$\hat{b}_1 = \frac{1}{\sqrt{2}} (\hat{a}_1 + i\hat{a}_2) \quad \hat{b}_2 = \frac{1}{\sqrt{2}} (\hat{a}_1 - i\hat{a}_2) \quad (\text{A.17})$$

Such that $\hat{L}_z = \hbar\hat{l}$ and $\hat{H} = \hbar\omega(\hat{n} + \hat{\mathbb{1}})$ for $\hat{l} = \hat{b}_2^\dagger\hat{b}_2 - \hat{b}_1^\dagger\hat{b}_1$ and $\hat{n} = \hat{b}_1^\dagger\hat{b}_1 + \hat{b}_2^\dagger\hat{b}_2$ [8].

A.4 Two-Particle Solution in Polar Coordinates

A.4.1 Decoupling the Hamiltonian

Now we add a second particle into the harmonic oscillator. As seen in Equation A.18 we've introduced a Coulomb interaction of strength λ , in addition to the harmonic potential on each particle .

$$H = \left[\frac{\hat{\mathbf{p}}_1^2}{2m_1} + \frac{\hat{\mathbf{p}}_2^2}{2m_1} \right] + \left[\frac{1}{2}m_1\omega^2\hat{\mathbf{r}}_1^2 + \frac{1}{2}m_2\omega^2\hat{\mathbf{r}}_2^2 \right] + \frac{\lambda}{|\hat{\mathbf{r}}_1 - \hat{\mathbf{r}}_2|} + H_{\text{spin}} \quad (\text{A.18})$$

Following Ref. [6], we shift to the relative and center-of-mass coordinates. Classically this transformation is given by Equations A.19 and A.20 respectively.

$$M = m_1 + m_2 \quad \mathbf{R} = \frac{m_1\mathbf{r}_1 + m_2\mathbf{r}_2}{m_1 + m_2} \quad \mathbf{P} = \mathbf{p}_1 + \mathbf{p}_2 \quad (\text{A.19})$$

$$\mu = \frac{m_1m_2}{m_1 + m_2} \quad \mathbf{r} = \mathbf{r}_1 - \mathbf{r}_2 \quad \mathbf{p} = \frac{m_2\mathbf{p}_1 - m_1\mathbf{p}_2}{m_1 + m_2} \quad (\text{A.20})$$

It straightforward to show that:

$$\frac{\mathbf{p}_1^2}{2m_1} + \frac{\mathbf{p}_2^2}{2m_2} = \frac{\mathbf{P}^2}{2M} + \frac{\mathbf{p}^2}{2m} \quad m_1\mathbf{r}_1^2 + m_2\mathbf{r}_2^2 = M\mathbf{R}^2 + \mu\mathbf{r}^2$$

Furthermore, this is a classically canonical change of variables as it conserves the Poisson bracket relationships. Therefore, the classical Hamiltonian can be reinterpreted as representing two particles with positions \mathbf{r} and \mathbf{R} and momenta \mathbf{p} and \mathbf{P} respectively.

Quantizing the system, we inherit the commutation relationships, the only non-zero commutators being $[\hat{r}_j, \hat{p}_j] = [\hat{R}_j, \hat{P}_j] = i\hbar$ for $j \in (x, y)$. Noting that in polar coordinates the vector norm, $|\mathbf{x}|$, equals the axial distance, ρ_x , we can decouple the quantum mechanical Hamiltonian as in Equation A.21

$$H = \underbrace{\left[-\frac{\hbar^2}{2\mu}\nabla_r^2 + \frac{1}{2}\mu\omega^2\rho_r^2 + \frac{\lambda}{\rho_r} \right]}_{H_r} + \underbrace{\left[-\frac{\hbar^2}{2M}\nabla_R^2 + \frac{1}{2}M\omega^2\rho_R^2 \right]}_{H_R} + H_{\text{spin}} \quad (\text{A.21})$$

This decoupled form of Equation A.21 allows for a product ansatz for the stationary states: $\psi(\mathbf{r}, \mathbf{R}, \mathbf{S}_1, \mathbf{S}_2) =$

$\xi(\mathbf{r})\Xi(\mathbf{R})\chi(\mathbf{S}_1, \mathbf{S}_2)$, where \mathbf{S}_j is the spinor for particle j . The corresponding eigenvalues have the form $E = \epsilon + \eta + E_{spin}$, where η and ϵ are the eigenvalues of H_R and H_r respectively.

Pauli's exclusion principle demands that if $\xi(\mathbf{r})$ is spatially symmetric with respect to the inversion $\mathbf{r} \rightarrow -\mathbf{r}$, then $\chi(\mathbf{S}_1, \mathbf{S}_2)$ must be spin-symmetric, and vice versa. There aren't any restrictions imposed on $\Xi(\mathbf{R})$. As such, the solutions to $\Xi(\mathbf{R})$ are identical to the single particle solutions given by Equations A.9 and A.10.

A.4.2 Analytical Solutions for the Internal Motion

The Schrödinger equation $H_r\xi(\mathbf{r}) = \epsilon\xi(\mathbf{r})$ can be expanded as in Equation A.22. For convenience, we ignore the subscript on the coordinates $\{\rho_{\mathbf{r}}, \phi_{\mathbf{r}}\}$.

$$\left\{ -\frac{\hbar^2}{2\mu} \left[\frac{1}{\rho} \frac{\partial}{\partial\rho} \left(\rho \frac{\partial}{\partial\rho} \right) + \frac{1}{\rho} \frac{\partial^2}{\partial\phi^2} \right] + \frac{1}{2}\mu\omega^2\rho^2 + \frac{\lambda}{\rho} \right\} \xi(\rho, \phi) = \epsilon \xi(\rho, \phi) \quad (\text{A.22})$$

Similar to the single-particle case, we can isolate the azimuthal factor in the wavefunction as $\Phi_l(\phi) = e^{\pm il\phi}$. Just as before, the azimuthal equation is equivalent to the eigenvalue relationship for the angular momentum. Therefore, l represents the number of angular-momentum quanta within the wavefunction. The radial equation is similar to Equation A.7 just with an additional Coulomb repulsion term.

$$0 = \left[\frac{d^2}{d\rho^2} + \frac{1}{\rho} \frac{d}{d\rho} - \frac{l^2}{\rho^2} \right] R(\rho) + \frac{2\mu}{\hbar^2} \left[\epsilon - \frac{1}{2}\mu\omega^2\rho^2 - \frac{\lambda}{\rho} \right] R(\rho) \quad (\text{A.23})$$

Following Ref. [6], we assume a solution of the form $R(\rho) = u(\rho)/\sqrt{\rho}$. Then $u(\rho)$ satisfies the Schrödinger equation given by Equation A.24

$$\left[-\frac{d^2}{d\rho^2} + \left(l^2 - \frac{1}{4} \right) \frac{1}{\rho^2} + \tilde{\omega}^2\rho^2 + \frac{\tilde{\lambda}}{\rho} \right] u(\rho) = \tilde{\epsilon}u(\rho) \quad (\text{A.24})$$

where we've defined $\tilde{\omega} = \mu\omega/\hbar$, $\tilde{\lambda} = 2\mu\lambda/\hbar^2$, and $\tilde{\epsilon} = 2\mu\epsilon/\hbar^2$. Switching to the dimensionless coordinate, $x \equiv \sqrt{\tilde{\omega}}\rho$, the radial Schrödinger equation reads as in Equation A.25.

$$\left[-\frac{d^2}{dx^2} + \left(l^2 - \frac{1}{4} \right) \frac{1}{x^2} + x^2 + \left(\frac{\tilde{\lambda}}{\sqrt{\tilde{\omega}}} \right) \frac{1}{x} \right] u(x) = \left(\frac{\tilde{\epsilon}}{\tilde{\omega}} \right) u(x) \quad (\text{A.25})$$

We clearly see that the system is only dependant on two dimensionless parameters: the coupling constant $\lambda^* \equiv \tilde{\lambda}/\sqrt{\tilde{\omega}}$ and the reduced energy $\epsilon^* \equiv \tilde{\epsilon}/\tilde{\omega}$.

When $x \rightarrow \infty$, the system resembles a harmonic oscillator (i.e. $u(x) \approx e^{\frac{1}{2}x^2}$). In contrast, when $x \rightarrow 0$ the system resembles a Hydrogen atom (i.e. $u(x) \approx x^{|l|+\frac{1}{2}}$). Therefore, we expect the analytical solutions to have the form given by Equation A.26, where $t(x)$ is a polynomial which

follows the differential equation A.27 [6, 7].

$$u(x) = e^{-\frac{1}{2}x^2} x^{|l|+\frac{1}{2}} t(x) \quad \text{where } t(x) \equiv \sum_{j=0}^{\infty} c_j x^j \quad (\text{A.26})$$

$$[\epsilon^* - 2(|l| + 1)] xt(x) - \lambda^* t(x) + (2|l| + 1)t'(x) - 2x^2 t'(x) + xt''(x) = 0 \quad (\text{A.27})$$

Solving this differential equation, we observe that the coefficients of the polynomial expansion, $\{c_j\}_{j \geq 0}$ follow a two-step recursion relation given by Equation A.28 [6].

$$c_0 = \text{normalization constant} \quad (\text{A.28a})$$

$$c_1 = \frac{1}{(2|l| + 1)} \frac{\tilde{\lambda}}{\sqrt{\tilde{\omega}}} c_0 \quad (\text{A.28b})$$

$$c_j = \frac{1}{j(2|l| + j)} \left\{ \frac{\tilde{\lambda}}{\sqrt{\tilde{\omega}}} c_{j-1} + \left[2(j + |l| - 1) - \left(\frac{\tilde{\epsilon}}{\tilde{\omega}} \right) \right] c_{j-2} \right\} \quad (\text{A.28c})$$

By induction, we see that any coefficient can be expressed as $c_j = F_j(|l|, \epsilon^*, \lambda^*)c_0$. To normalize the wavefunction we truncate the power-series at $j = m$. This corresponds to the conditions given by Equation A.29 [6, 7].

$$c_m = 0 \iff F_m(|l|, \epsilon^*, \lambda^*) = 0 \quad (\text{A.29a})$$

AND

$$c_{m+1} = 0 \iff \frac{\tilde{\epsilon}}{\tilde{\omega}} = 2(|l| + m) \quad (\text{A.29b})$$

As suggested by Ref. [6], these equations simultaneously determine the allowed spectrum. We first calculate the solvable fields $\tilde{\lambda}^2/\tilde{\omega}$ from A.29a for a particular m and $|l|$. We insert the corresponding values of $\tilde{\omega}$ into A.29b to determine the energy-values [6]. The true energies for the solvable values of $\tilde{\omega}$ are given by Equation A.30. Unlike the non-interacting system, the ground-state of this system is at zero.

$$\epsilon = \hbar\omega(|l| + m) \quad (\text{A.30})$$

The exact solutions of the interacting system can be categorized in two groups: infinite-field solutions, where $\tilde{\lambda}^2/\tilde{\omega} = 0$, and finite-field solutions, where $\tilde{\lambda}^2/\tilde{\omega} > 0$ [6, 7]. Note that the wavefunctions below are given as a function of the axial distance, ρ rather than the dimensionless distance x .

For $m = 1$, there is only one infinite-field solution given by Equation A.31

$$\frac{\tilde{\lambda}^2}{\tilde{\omega}} = 0 \implies t_{2,l}(\rho) = 1 \quad (\text{A.31})$$

For $m = 2$, there is one finite-field solution given by Equation A.32

$$\frac{\tilde{\lambda}^2}{\tilde{\omega}} = 2(2|l| + 1) \implies t_{2,l}(\rho) = 1 + \left(\frac{\tilde{\lambda}}{2|l| + 1} \right) \rho \quad (\text{A.32})$$

For $m = 3$, there is one infinite and one finite-field solution given by Equation A.33

$$\frac{\tilde{\lambda}^2}{\tilde{\omega}} = 0 \implies t_{3,l}(\rho) = 1 - \left(\frac{\tilde{\omega} \rho^2}{|l| + 1} \right) \quad (\text{A.33a})$$

$$\frac{\tilde{\lambda}^2}{\tilde{\omega}} = 4(4|l| + 3) \implies t_{3,l}(\rho) = 1 + \left(\frac{\tilde{\lambda} \rho}{2|l| + 1} \right) + \left(\frac{\tilde{\lambda}^2 \rho^2}{2(2|l| + 1)(4|l| + 3)} \right) \quad (\text{A.33b})$$

For finite-fields, $\tilde{\omega}$ is exactly solvable in terms of $\tilde{\lambda}^2$. Substituting these values of $\tilde{\omega}$ into Equation A.30 gives the energyvalues as a function of the squared e-e interaction strength, $\tilde{\lambda}^2$.

On the other hand, the wavefunctions within infinite-fields do not depend on $\tilde{\lambda}$ at all. If we assume a finite frequency oscillator ($\tilde{\omega} < \infty$), then these correspond to a vanishing electron-electron interaction ($\tilde{\lambda} \rightarrow 0$). Section A.4.3 below shows that these solutions exactly resemble the single-particle solutions.

A.4.3 Infinite-Field Solutions

Comparison of Equations A.10 and A.30, shows that the interacting system is degenerate with the non-interacting one for odd values of m (i.e. $m = 2n + 1$). Odd values of m are also the only ones which produce infinite-field solutions. Intuitively, the limit $\tilde{\lambda}/\sqrt{\tilde{\omega}} \rightarrow 0$ corresponds to either a very thin and steep well potential or a negligible electron-electron repulsion. Either way, we expect the electrons to be confined close to the origin, qualitatively resembling the behavior of a single electron.

Consider the solution described by Equations A.26 and A.28. Substituting $\tilde{\lambda}/\sqrt{\tilde{\omega}} = 0$ we realize that only even-indexed coefficients are non-zero. This implies that $t(x)$ is a function of x^2 only. If we insert $m = 2n + 1$ and $j = 2k$ into A.28 we obtain the recursion relation for the generalized Laguerre polynomial $L_n^{|l|}(x^2)$ given by Equation A.34 [7]. This shows that the eigensolutions corresponding to $\tilde{\lambda}/\sqrt{\tilde{\omega}} = 0$ are equivalent to those given by Equation A.9.

$$c_k = \frac{(k - n - 1)}{k(k + |l|)} c_{k-1} \quad (\text{A.34})$$

In summary, the set of solutions for the non-interacting Hamiltonian are contained within the set of exactly solvable solutions of the interacting system. In the limit of an infinitely steep well and no mutual repulsion, the electrons are forced to densely pack themselves at the origin.

A.4.4 Finite-Field Solutions

Now we turn our attention to the solutions for which $\tilde{\lambda}/\sqrt{\tilde{\omega}} > 0$. Figure A.5 plots the energy spectrum of the solvable states versus the coupling coefficient squared. Figure A.6 plots the wavefunctions for some of these states. We can group the solvable states based on the number of nodes in the corresponding wavefunction (i.e. the excitation number), forming energy bands (colored lines) as a function coupling coefficient. If we index these bands as n , we notice that this exactly corresponds to the relationship $m = 2n + 1$ when $\tilde{\lambda}/\sqrt{\tilde{\omega}} = 0$. In other words, the infinite-field (single-particle) solutions evolve with the coupling parameter. The solvable states along a band are exactly those where $\tilde{\epsilon}/2\tilde{\omega} = |l| + m$ is an integer. This exactly aligns with the requirement for the truncation of the power-series at some integer m .

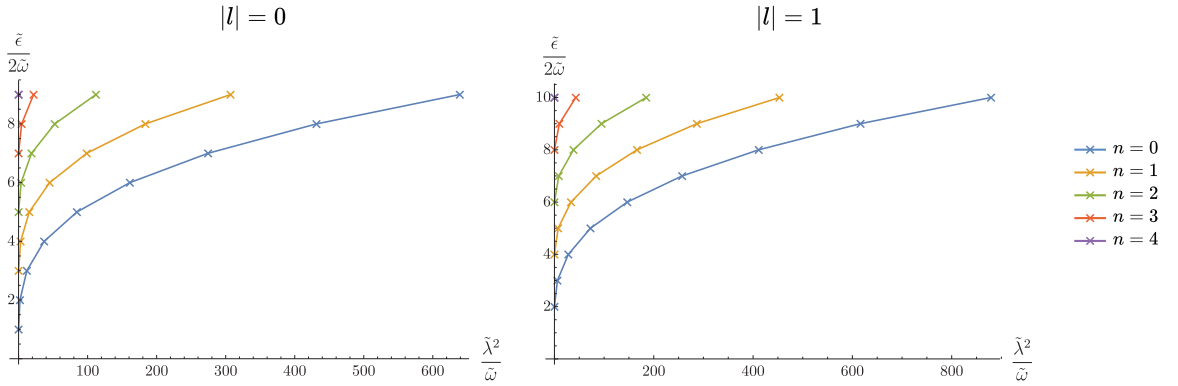


Figure A.5: Energy spectra for the solvable states versus the coupling coefficient squared, for $|l| = 0$ and $|l| = 1$. The states are grouped (colors) based on the number of nodes, n in the corresponding wavefunctions. This forms the energy bands (colored lines) as a function of the coupling coefficient. Generated using Mathematica.

Figure A.7 compares the ground-states (lowest solvable ω) for various values of m . Classically, the particle is expected to be at the minima, ρ_0 of the effective potential. Therefore, the distance is given in units of ρ_0 . Observe that as we increase m , the corresponding ground-state frequency decreases (as expected from the blue line in Figure A.5). This corresponds to a thin-and-steep well or minimal repulsion between the electrons, which is reflected by the wavefunction becoming increasingly concentrated around ρ_0 .

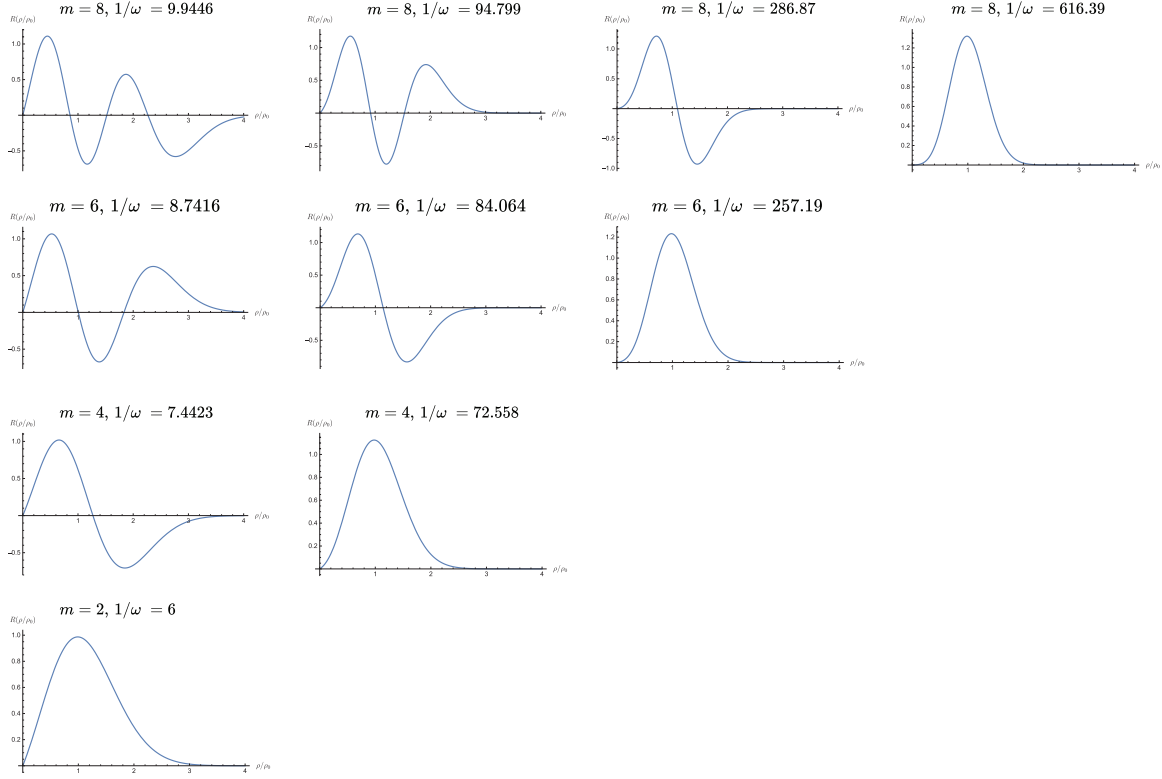


Figure A.6: Wavefunctions for some of the solvable states for $|l| = 1$. Note that we've ignore the states corresponding to odd values of m as they qualitatively resemble the adjacent even energy levels for $m' = m - 1$. The distance is given in units of ρ_0 . Generated using Mathematica.

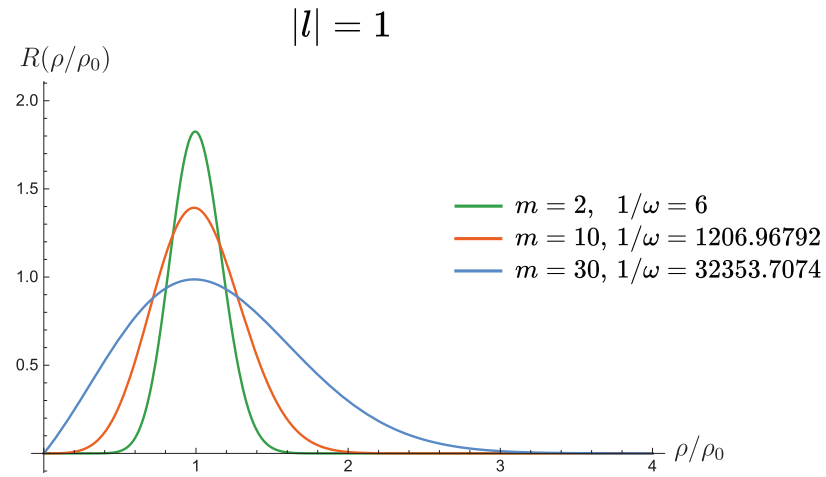


Figure A.7: Comparing the ground-states for $m = 2$ (blue), $m = 10$ (orange), and $m = 30$ (green).The distance is given in units of ρ_0 . Generated using Mathematica.

B

Detailed Description on the Heidelberg Dose Tests

To perform these tests we tile a 100×100 array of quantum dots across 17 columns and 7 rows. Across the columns we sweep the intensity of the laser, from 20% to 100%, with increments of 10%. Down the rows we sweep the focus-offset of the laser, from 0% to 15% with increments of 2.5%. Unless otherwise specified, photolithography is performed using the 2mm writehead on AZ1505 photoresist spun at 4000rpm for 40s.

Table B.1: Fabrication Steps to Define the Bond-Pads and Dice the Devices

Sample Number	Difference in Fabrication from Initial	Comments
HDT010 (Initial Device)	<ul style="list-style-type: none"> • Default stripe width of $60\mu\text{m}$ • Filter: 1 % • 1 min develop • No Aluminum Hard Mask 	The dots are wide visibly wider than expected, although they do not merge into one another.
HDT011	<ul style="list-style-type: none"> • Filter: 1 % + 25 % • 1 min develop • No Aluminum Hard Mask 	The larger features are well defined but no dots have been defined, even for the highest intensity doses.
HDT020	<ul style="list-style-type: none"> • Filter: 1 % • 5 min develop • Aluminum hard mask present 	We can see dots only for the dose corresponding to the highest intensity and focus offset. We see a gradient in the size of the dots across a row, as well as a stitching error between consecutive stripes. Optial and SEM images from this sample are shown in Figure 3.4.

HDT030

- Filter: 1 % + 25 %
- No Aluminum Hard Mask
- AZ1505 Photoresist spun at 6000rpm for 40s

We thought that a thinner layer of photoresist may be able to produce dots. While we were able to see the larger features defined within the resist, no dots could be seen. This further proves that an aluminum hard mask with a longer develop time is the most promising way forward.

HDT021

- Stripe width changed to 20 μm
- Filter: 1 % Only
- Aluminum hard mask present
- 5 min develop

After HDT020, we hoped to make the laser more intense. However, making the stripe-width narrower as well as removing the 25% filter added up to make the laser stronger than required. As seen in Figure 3.5, the dots are significantly overdeveloped. We can correct for this with additional filters and a shorter develop time.

HDT022

- Stripe width changed to 20 μm
- Filter: 1 % + 50 %
- Aluminum hard mask present
- 3 min develop

The dots are distinguishable for nearly all doses. We see a gradual variance in the size of dots as the intensity increases; from the smallest dots of width 650nm to doses where the dots have merged to form anti-dots. This change in size is shown by the SEM images in Figure 3.6. We see some chipping around the dots in the aluminum hard mask. This isn't defined into the TaWSi layer. This could possibly be avoided by reducing the laser's intensity.

HDT023

- Stripe width changed to 20 μm
- Filter: 1 % + 25 %
- Aluminum hard mask present
- 3 min develop

This set of dose-tests could not be fabricated due to time constraints. We expect this sample to be the best so far, with the smallest sized dots and minimal chipping in the aluminum.

C

Engineering and Industrial Standards

The independent project described in this thesis incorporated the following engineering and industrial standards:

Standardized modeling conventions: AutoCAD software package was used to design the CAD files used for photolithography. FlexPDE was used for the finite-element modelling of the dots.

International units of physical quantities: SI units were used throughout the thesis.

Programming languages: Mathematica was used to compute the wavefunctions and energy-values of the 2D harmonic oscillator and related quantum mechanical problems.

Bibliography

- [1] L. P. Kouwenhoven, D. G. Austing, and S. Tarucha. Few-electron quantum dots. *Reports on Progress in Physics*, 64(6):701–736, 2001.
- [2] Gordon Baym. *Lectures On Quantum Mechanics*. New York: W.A. Benjamin, 1969.
- [3] M. A. Armstrong. *Groups and Symmetry*. Springer, New York, NY, 1988.
- [4] E Rousseau, D Ponarine, Y Mukharsky, O Avenel, and J M Richomme. To Quantum Dots and Qubits with electrons on helium.
- [5] G. Papageorgiou, P. Glasson, K. Harrabi, V. Antonov, E. Collin, P. Fozooni, P. G. Frayne, M. J. Lea, D. G. Rees, and Y. Mukharsky. Counting individual trapped electrons on liquid helium. *Applied Physics Letters*, 86(15):1–3, apr 2005.
- [6] M. Taut. Two electrons in a homogeneous magnetic field: Particular analytical solutions. *Journal of Physics A: Mathematical and General*, 27(3):1045–1055, feb 1994.
- [7] M. Taut. Special analytical solutions of the Schrödinger equation for two and three electrons in a magnetic field and ad hoc generalizations to N particles. *Journal of Physics Condensed Matter*, 12(15):3689–3710, apr 2000.
- [8] E Karimi, R W Boyd, P De La Hoz, H De Guise, J Řeháček, Z Hradil, A Aiello, G Leuchs, and L L Sánchez-Soto. Radial quantum number of Laguerre-Gauss modes. 2014.
- [9] Ramamurti Shankar. *Principles of Quantum Mechanics*. Springer, New York, NY, 2 edition, 1994.